Comparative Study of Mask Architectures for EUV Lithography

Adam R. Pawloski[*a], Bruno La Fontaine[a], Harry J. Levinson[a], Stefan Hirscher[b], Siegfried Schwarzl[b], Klaus Lowack[b], Frank-Michael Kamm[b], Markus Bender[b], Wolf-Dieter Domke[b], Christian Holfeld[c], Uwe Dersch[c], Patrick Naulleau[d], Florian Letzkus[e], Joerg Butschke[e]

[a]Advanced Micro Devices, One AMD Place, P.O. Box 3453, Sunnyvale, CA, USA 94088
[b]Infineon Technologies AG, Balanstrasse 73, 81541 Munich, Germany
[c]Advanced Mask Technology Center, Raehnitzer Allee 9, 01109 Dresden, Germany
[d]Lawrence Berkeley National Lab, Berkeley, CA, USA 94720
[e]IMS-Chips, Allmandring 30a, 70569 Stuttgart, Germany

ABSTRACT

Three different architectures were compared as candidates for EUV lithography masks. Binary masks were fabricated using two different stacks of absorber materials and using a selective etching process to directly pattern the multilayer of the mask blank. To compare the effects of mask architecture on resist patterning, all three masks were used to print features into photoresist on the EUV micro-exposure tool (MET) at Lawrence Berkeley National Laboratory. Process windows, depth of focus, mask contrast at EUV, and horizontal and vertical line width bias were use as metrics to compare mask architecture. From printing experiments, a mask architecture using a tantalum nitride absorber stack exhibited the greatest depth of focus and process window of the three masks. Experimental results obtained using prototype masks are discussed in relation to simulations. After accounting for CD biasing on the masks, similar performance was found for all three mask architectures.

Keywords: extreme ultraviolet lithography, mask architecture, etched multilayer binary mask, TaN absorber

1. INTRODUCTION

Extreme ultraviolet lithography (EUVL) uses reflective photomasks with an oblique illumination angle, resulting in imaging characteristics at the wafer that differ from those of conventional optical lithography. These imaging characteristics, unique to the reflective optics for EUVL, create an additional level of complication for sizing mask features correctly in order to achieve a given pattern in photoresist at the wafer. Several groups have studied the interplay of the patterned mask structure with the oblique illumination.[1-3] For example, the topography of an absorber film on top of a reflective mask blank can cause shadowing of the projected image into resist for lines that run perpendicular to the direction of the oblique illumination, resulting in horizontal and vertical (H-V) CD bias at the wafer. The impact of shadowing caused by mask architecture is related to the height of the absorber stack, the angle of the absorber sidewall, and the composition of the absorber material. One possible solution to eliminate H-V bias due to mask architecture is to directly pattern the multilayer reflector of the mask blank. The advantages of patterned reflector masks have been described in previous work.[1, 4, 5] In addition to minimizing H-V bias, larger process windows, less sensitivity to variation of pattern dimensions and sidewall angle, and a larger contrast at the actinic wavelength were all observed through simulation. Although it may be possible to use mask CD biasing to correct for H-V bias at the wafer when using patterned absorber mask architecture, the patterned reflector mask architecture also offers an improved process window. In the event that fabrication of etched multilayer binary masks (EMBM) for EUV prove too difficult or costly, it may also be possible to enhance imaging performance by the adoption of absorber stack materials different from the prevalent chromium absorber. Materials based on tantalum nitride (TaN) have been explored as possible alternate absorbers for photomask applications.[6-13] Optimization of the absorber film thickness and selection of high contrast materials at the target EUV wavelength will improve overall imaging performance, including larger process window. For these reasons, the investigation of architecture for EUV photomasks remains an active area of research.

An experimental comparison between patterned absorber and patterned reflector masks was previously attempted on a 0.1NA EUV stepper, but the poor control of the tool and of the resist process prevented the authors from clearly verifying the predicted advantages of the patterned reflector masks.[4] A new set experiments aimed at comparing these types of architectures is presented in this paper. In particular, we have investigated absorber masks with a TaN/SiO_2 and a Cr/SiO_2 absorber stacks and a patterned reflector mask. The main goal of the work presented in this paper is to understand the advantages and disadvantages of these different EUV mask architectures. Our approach relies on the printing of prototype masks in resist at EUV to test their performance in terms of process latitude and sensitivity to different imaging parameters. These results are sought to validate and calibrate our simulation models. Once simulation tools have been shown to exhibit predictive accuracy, they will be used to identify the optimum mask architecture for EUV lithography at the expected insertion technology node, with production specifications. Moreover, fabrication of prototype masks using both patterned absorber and patterned reflector architectures has advanced our appreciation and skill for making these types of masks.

2. MASK FABRICATION

Three prototype, binary EUV photomasks were investigated in this work, and included two patterned absorber masks and one etched multilayer mask. A summary of the mask architectures can be found in Table 1. The first patterned absorber mask consisted of a 70nm chromium absorber film over 20nm of SiO_2 used as the buffer layer. This mask was not fabricated by the authors, but was produced by members of International SEMATECH and Lawrence Berkeley National Laboratory (LBNL) for use with the EUV micro-exposure tool (MET). The other two masks were fabricated at the Advanced Mask Technology Center (AMTC) in Dresden, Germany in collaboration with IMS Chips in Stuttgart, Germany. The second absorber mask had a 70nm TaN absorber film over 60nm of SiO_2 buffer layer. Figure 1 demonstrates the process flow used for manufacturing the TaN absorber mask. The third mask, an etched multilayer mask, was fabricated by direct patterning of the multilayer blank. In this process, described in Figure 2, a film of chromium was used as a hard mask for dry etching of the multilayer. All three masks were fabricated using high-resolution e-beam lithography.

Table 1. Description of Mask Architectures

Absorber	Absorber thickness (nm)	Buffer layer	Buffer layer thickness (nm)	Total height of stack (nm)	Transmission of the stack (%)	Aerial image contrast (%)
Cr	70	SiO2	20	90	0.44	98.8
TaN	70	SiO2	60	130	0.11	99.4
Etched Mo/Si	280	---	---	280	N/A	99.97

The MET was designed as a 5× reduction system. The illuminated field size at the wafer is limited to 200μm by 600μm, or 1mm by 3mm at the mask. Due to the small image field size, the mask layout was partitioned into an array of 35 unique subfields that could be patterned individually. All masks contained one identical subfield in their layout that was used for comparison of the three mask architectures. This subfield, designed by LBNL, consisted of a variety of line and space resolution patterns through pitch and line width. Due to an error in defining mask parity for the etched multilayer mask, the resulting image in resist was flipped across the horizontal axis compared to the absorber masks. This did not affect the definition of horizontal and vertical features on the mask and should not have had an effect on imaging results since the pattern density was exactly the same.

In the MET, capacitance gauges are used to control reticle positioning. In order for these gauges to work properly, the front side of the photomask must be made from a conductive film. For absorber mask fabrication, this is easily met by keeping the vast majority of the mask periphery covered in absorber to create a mainly dark tone. For the case of the etched multilayer mask, this can be accomplished by keeping the multilayer intact across the mask periphery, however this would result in mainly a bright-field tone. In order to minimize any chance that the difference in tone could lead to greater magnitude of long range flare, the etched multilayer mask was fabricated using two lithography write steps in order to keep the chromium hardmask covering the periphery. The first write process defined the hardmask pattern that was used to etch the high-resolution features in the printing subfields. The second write process defined the regions in the chromium hardmask to be removed.

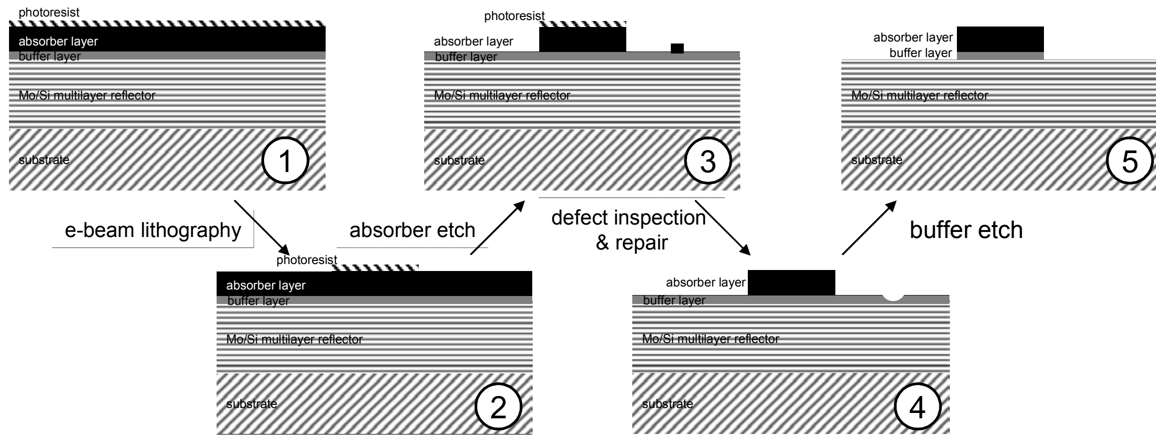

Figure 1. Main processing steps for the fabrication of patterned absorber masks. 1- Initial mask blank composed of the substrate, the Mo/Si multilayer film that provides high reflectance at 13.4 nm, a buffer layer, an absorber layer, and finally the photoresist film. 2- Mask blank after e-beam lithography. 3- Mask blank after absorber etch, showing a sample defect in the form of a small absorber residue. 4- Mask blank after defect inspection and repair. The role of the buffer layer here is to protect the underlying multilayer from being affected by the repair process (*e.g.*, focused ion beam repair). 5- Final patterned mask.

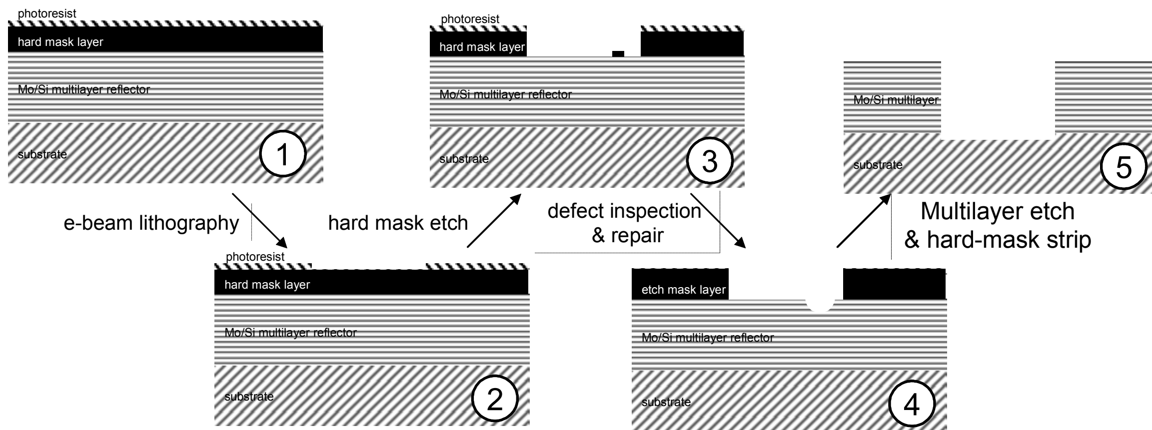

Figure 2. Main processing steps for the fabrication of patterned reflector masks. 1- Initial mask blank composed of the substrate, the Mo/Si multilayer film that provides high reflectance at 13.4 nm, a hard-mask layer, and finally the photoresist film. 2- Mask blank after e-beam lithography. 3- Mask blank after hard-mask etch, showing a sample defect in the form of a small absorber residue. 4- Mask blank after defect inspection and repair. Note that there is no need for a buffer layer in this case since the underlying multilayer film will be etched away at the next processing step anyway. 5- Final patterned mask.

CD measurements were made on each of the masks using SEM metrology. SEM micrographs were analyzed for CD using the image analysis software SuMMIT (EUVL Technology[14]). Measurements for target features are reported in Table 2. The CD for patterned absorber and patterned reflector masks followed the convention defined in Figure 3. By this convention, the CD of a patterned absorber mask is defined by the bottom CD of the absorber line. Conversely, the CD of the patterned reflector is defined by the distance between top CDs of the multilayer patterns. For the etched multilayer mask, the sidewall angle was estimated by geometrical construction after measuring the top and bottom CDs of the multilayer features for a given pitch and known thickness of multilayer. The sidewall angle for the target 60nm features was estimated as 77.5^{o}. Figure 4 displays SEM images obtained for the three prototype photomasks.

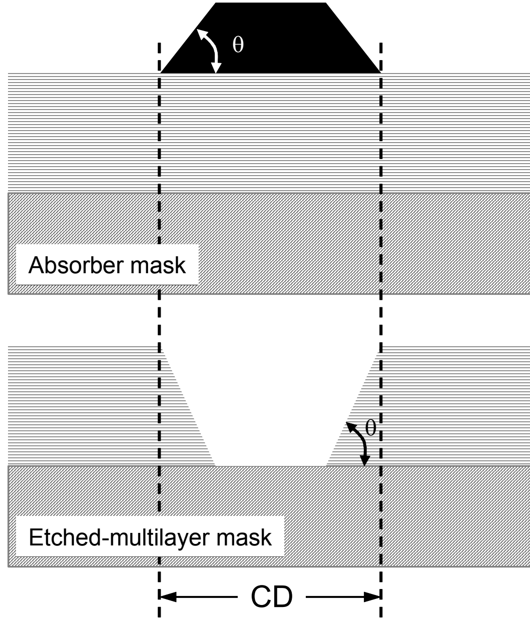

Figure 3. Schematic description of the cross-section of both an absorber mask and an etched multilayer mask. We define the critical dimension (CD) of the mask patterns as the bottom CD for absorber mask and as the top CD for the etched multilayer mask. The sidewall angle, θ, is defined as the angle between the top of the multilayer and the sidewall of the absorber stack for the absorber mask, and as the angle between the substrate and the sidewall of the multilayer film for the etched multilayer mask.

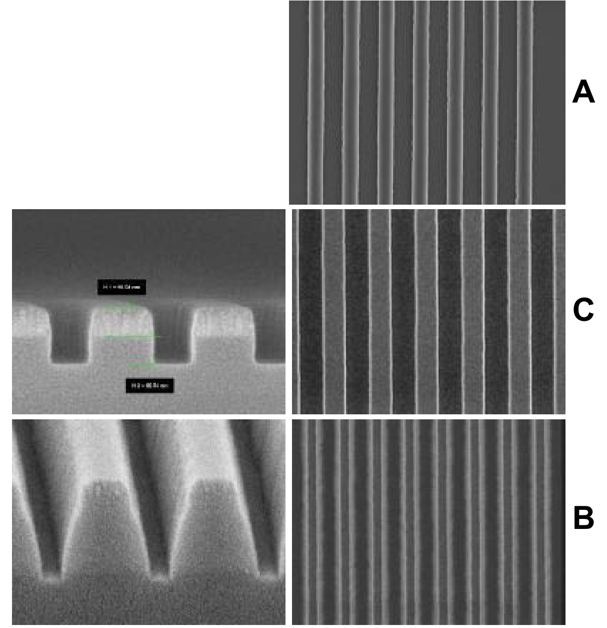

Figure 4. SEM micrographs of masks used in this experiment. a) 60nm (at wafer) vertical lines on the Cr/SiO_2 mask, b) 60nm vertical lines on the TaN/SiO_2, and c) 70nm vertical lines on the etched multilayer mask. Top-down SEM images are from actual masks used for printing. Cross-section images were taken from plates used for process development. The etched multilayer mask is shown after a partial multilayer etch with the chromium hardmask still intact.

3. SIMULATION

In this paper, rigorous electromagnetic simulation methods are applied to mask scattering and imaging by using the software package EM-suite from Panoramic Technology.[15] Köhler illumination is assumed at the source plane. Diffraction of light at the mask is simulated by solving Maxwell's equations with the finite difference time domain algorithm TEMPEST. Full 2D multilayer mask models are used in the mask electromagnetic scattering process. A vector diffraction model is used to simulate light diffraction in the imaging optics system from the object plane to the imaging plane. Finally the aerial images are calculated in air at the wafer plane. The resist processes are not simulated in this paper and a threshold model is used to calculate CDs.

In etched multilayer mask simulations, the multilayer structure is assumed to have 40 Mo and Si bilayer pairs and simulated rigorously. For absorber mask simulations, a reflective Fourier boundary layer is used instead of the full multilayer film stack to improve computational speed. All simulations have a fixed node size $dx = dy = dz = 0.7$ nm. Periodic boundary conditions are applied to the X and Y boundaries and a perfectly absorbing matching layer is used as the Z boundary conditions. Dense lines on a 120 nm pitch are simulated both for horizontal and vertical orientations and for a range of mask CDs. The imaging system has a numerical aperture NA = 0.3 and is described by the pupil map that was measured by Goldberg et al.[16] The illumination used in the simulations is annular with inner sigma of 0.3 and outer sigma of 0.7, which matches closely the experimental conditions. The demagnification factor is M = 5. The imaging plane is in the defocus range of –350 nm to 350 nm. The EUV radiation has the nominal wavelength 13.4 nm with a total 2% bandwidth window. The EUV light is incident from a cone centered at 4º from normal for the horizontal features and at a normal incidence for the vertical features. At the normal EUV wavelength, $\lambda = 13.4$ nm, the following refractive indices are used with extra digits of accuracy shown so that the exact results can be reproduced by others. Silicon has a refractive index of $0.999931 - j\times0.00182108$, molybdenum has a refractive index of 0.922739 –

j×0.00621991, chrome has a refractive index of 0.933328 – j×0.0381974, SiO_2 has a refractive index of 0.9787098 – j×0.0105698, and TaN has a refractive index of 0.9272115 – j×0.0429261.[17] The EUV radiation is excited at the top of domain. The reflection output plane is 5 nm above the excitation plane.

Figure 5 shows cross-sections of the simulated light intensity being reflected and scattered by the mask structures and profiles of the near-field intensity reflected by the masks. For all three mask studied, the dimension and sidewall angle of the structures used in the mask simulations are adjusted to fit that of the actual patterned masks. The Cr/SiO_2 mask is simulated using a 55 nm CD and 90° sidewall angle, the TaN/SiO_2 mask is simulated using a 65 nm CD and 90° sidewall angle, and the etched multilayer mask is simulated using a 60 nm CD and 80° sidewall angle.

Two main differences are observed in the near-field intensity. First, the near field image at the edge of the absorbers in Figure 5(a) and 6(b) exhibits greater amplitude of interference than the etched multilayer mask, shown in Figure 5(c). Second, the dark region for the etched multilayer mask shown in Figure 5(c) has lower contrast and some small interference effects that are not present in simulations of the absorber masks. The lower contrast and interference effects seen in the near-field intensity distribution for the etched multilayer mask are due to the reflectivity of the sidewalls of the multilayer mask. All of these effects occur on a very short scale and are mostly diffracted at angles larger than those captured by the imaging optics.

The aerial images corresponding to the three cases displayed in Figure 5 are plotted in Figure 6, using the MET aberrated pupil map and assuming best focus. One can observe that most of the differences observed at the near-field have now been filtered out by the imaging optics and the main difference left between the three cases is the width of the images, which matches that of the mask CDs. In previously published papers,[1, 5] we have reported that the quality of the aerial images produced by the etched multilayer mask was better than that of the absorber masks for the case where the sidewall of the etched multilayer mask was 90°. As observed here, a sidewall angle that is not as steep (*i.e.* 80°) deteriorates the quality of the aerial image produced by the etched multilayer mask to a level comparable to that of the absorber masks.

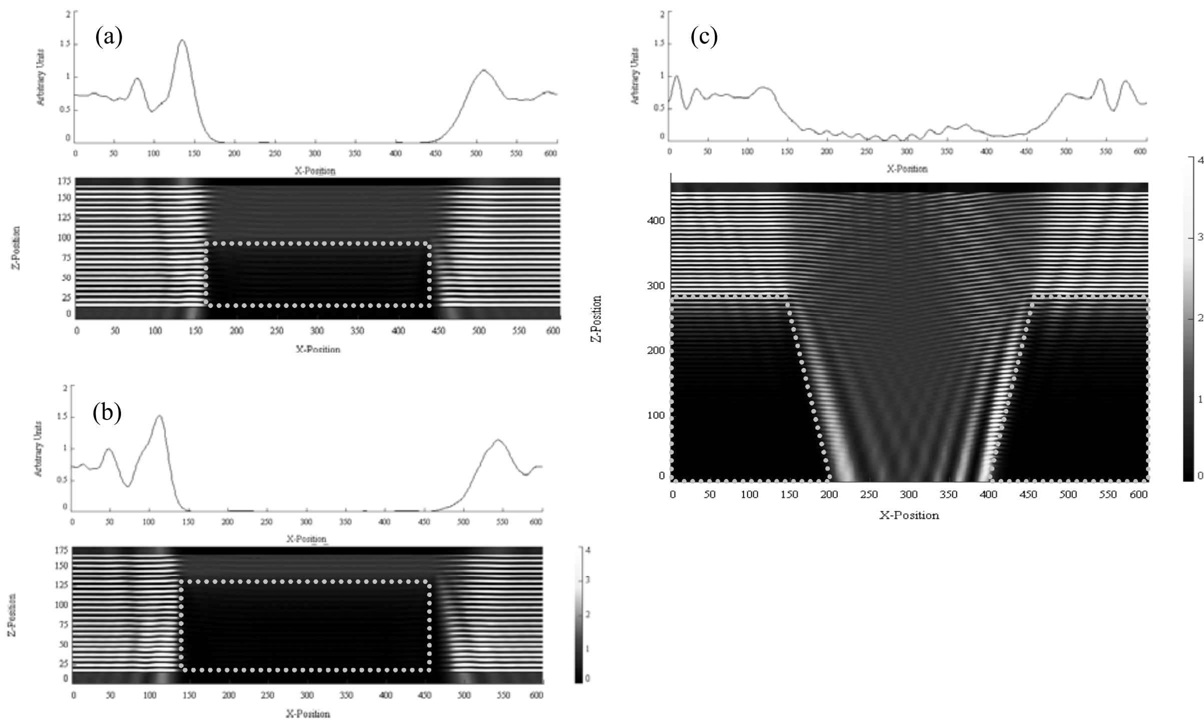

Figure 5. Near-field intensity cross-sections and profiles for the three masks studied as calculated by Tempest: (a) Cr/SiO_2 mask, (b) TaN/SiO_2 mask, and (c) etched multilayer mask. The Cr/SiO_2 mask is simulated using a 55 nm CD and 90° sidewall angle, the TaN/SiO_2 mask is simulated using a 65 nm CD and 90° sidewall angle, and the etched multilayer mask is simulated using a 60 nm CD and 80° sidewall angle.

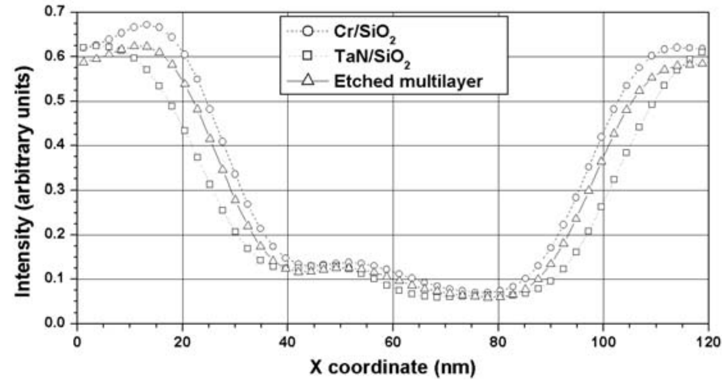

Figure 6. Aerial images of horizontal lines for the three masks under evaluation at best focus, as calculated using EM-Suite. The red curve corresponds to the Cr/SiO_2 mask (55 nm line), the blue curve is the aerial image of the TaN/SiO_2 mask (65 nm line), and the black curve is that of the etched multilayer mask (60 nm line). Dotted lines are added as a visual guide to locate the position of the 60 nm feature.

Bossung plots are obtained from the aerial images through focus by calculating the CD at a range of intensity levels, assuming a threshold model. The results are displayed in Figure 8. The main difference between the three cases is the iso-focal CD, which tends to shift with the CD on the mask but not exactly by the same amount. We will come back to this point in the discussion section.

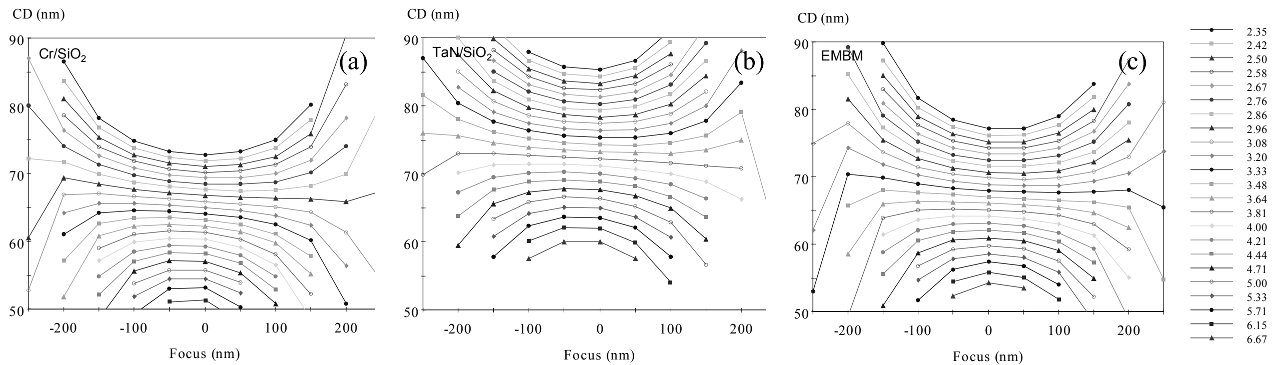

Figure 7. Simulated Bossung plots for (a) the Cr/SiO_2 mask, (b) the TaN/SiO_2 mask, and (c) the etched multilayer mask.

4. EUV PRINTING RESULTS

The three mask prototypes were imaged into photoresist at EUV using the MET at LBNL. The MET is a 0.3NA, 5× reduction system with a fully programmable pupil fill.[18] The source of radiation is from the Advanced Light Source (ALS), a synchrotron radiation source, and provides highly coherent, narrow band EUV radiation at 13.5 nm wavelength. Prior to assembly into an exposure station, visible light and at wavelength interferometry were performed to characterize aberrations for the optic. A reticle exchange port allows for masks to be switched inside the tool within about one hour of handling and alignment time. The system is equipped with precision focus leveling at the wafer and reticle planes. The flatness of each resist-coated wafer was mapped using the wafer height sensor prior to exposure, and a target region on the wafer was flattened across the 5 mm field by adjusting wafer tilt. Focus precision is better than 10nm at the mask, however focus does drift over time due to very subtle variations in the optics of the system, likely due to temperature changes. Dose control on the system is better than 2% variation from field to field. After a reticle is loaded into the system, the mask subfield to be imaged is located using coarse alignment marks on the reticle and a CCD camera. An internal dose sensor is used to verify the alignment of the illumination spot onto the subfield. This sensor was also used

to measure the EUV contrast of the photomasks. To measure contrast, the current on the dose sensor was measured while illuminating a subfield consisting of uncovered multilayer and a completely dark region of the mask absorber (or etched multilayer). Experimental measurement of mask contrast at EUV is shown in Table 2, and agrees with simulated values of contrast from Table 1, with contrast of the etched multilayer mask greater than the TaN/SiO_2 mask.

Annular illumination was used for printing experiments with outer and inner radii of 0.7 and 0.3, respectively. The photoresist MET-1K (XP3454) from Rohm Haas Microelectronics was used for all imaging experiments. MET-1K was chosen for these experiments based on early data from MET printing experiments indicating this resist was capable of resolution down to 35nm lines and spaces.[19] Resist was coated onto HMDS primed, 4-inch silicon substrates. The target film thickness was 125nm, the post-application bake (PAB) was at 130°C for 60s, the post-exposure bake (PEB) was at 130°C for 90s, and LDD26W developer was used for a 45s development. Wafers were exposed in focus-exposure matrices (FEM) using dose steps of 5% of the targeted dose to size (D_{size}), and 50nm steps in focus. Typical FEM sizes were 11 steps in dose and 13 steps in focus. Wafers were patterned with one, two, or three different FEMs on the same wafer using separate subfields. Prior to exposure of a FEM for data collection, a setup wafer was exposed using a coarse FEM (large focus and dose steps) under identical process conditions to estimate D_{size} and the position of best focus. The target features were the horizontal and vertical lines from the 60nm right angle elbows at 120nm pitch in the LBNL resolution bright field subfield. Micrograph images were recorded for horizontal and vertical lines using an Hitachi S-4800 scanning electron microscope (SEM) at 200kX magnification. After image capture, the software package SuMMIT (EUVL Technology[14]) was used to measure CDs from each image.

The photospeed for MET-1K is slower than its predecessor resist, EUV-2D, but resolution capabilities were 10-15nm improved for dense lines and spaces.[20, 21] The dose to size for 60nm lines and spaces was approximately 20mJ/cm^2. It was learned during the experiments that the resist MET-1K exhibited an iso-dense bias that was somewhat worse than EUV2D, based on observation of previous work. Due to the iso-dense bias of the resist, the outer lines of the resolution elbows decreased in line width at lesser exposure doses than the center lines of the group, as can be seen from the SEM images in Figure 8. This often led to complete elimination or pattern collapse of outer lines, and made analysis of isolated lines impossible for the range of dose values used during the printing experiments. To remove the effect of iso-dense bias from our data analysis of the dense lines of the resolution elbows, only the center line of the features was used to measure CD. The downside of this choice was increased variability due to fewer statistics, especially in the case of measuring line edge roughness, which requires large sample sizes and long lengths of lines for accurate results. A further complication of the resist process was control of the feature profile shape. Shown in Figure 8 are SEM micrographs for 60 nm vertical lines through dose printed with the TaN/SiO_2 absorber mask. It can be seen that at low values of dose the resist exhibits a foot, and at high values of dose the profile becomes rounded and has significant top loss. During measurements of CD, many of the overexposed images could not be used because measurement of CD for these images resulted in CDs that were erroneously too large since the top of the resist was gone and only the foot remained. It was also noted that large values of dose, in excess of 2-3 times the dose to size, the MET-1K resist began to exhibit negative-tone behavior, likely due to cross-linking under exposure to the high energy, ionizing radiation of EUV.

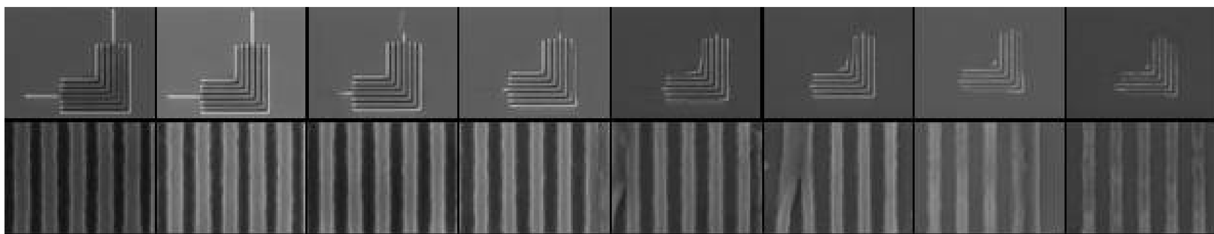

Figure 8. SEM micrographs of 60 nm elbows and vertical lines and spaces printed in MET-1K photoresist using the TaN/SiO_2 absorber mask (wafer 3) at a best focus and through dose from 18.8 to 28.8 mJ/cm^2, left to right in steps of 1.25 mJ/cm^2.

One challenge faced during resist printing on experimental exposure tools is the control of wafer-to-wafer repeatability. Repeatability is required in both tool performance and in resist processing in order to allow comparison of data collected on different wafers and during different days. For these experiments, we attempted to measure the repeatability of the

printing process in two ways. First, three identical FEMs were patterned onto the same wafer without removing the wafer from the tool or adjusting illumination and exposure conditions. After patterning, the three FEMs were inspected in the SEM to evaluate best dose and focus. From this exercise, the conditions of best focus and best dose did not change more than one step in focus (±50 nm) and dose (±1.1 mJ/cm^2). Second, repeatability was investigated by patterning the same FEM conditions on two different wafers. This was repeated for each mask type. As listed in Table 2, the value of D_{size} for vertical lines could change by more than 4 mJ/cm^2 from wafer to wafer although identical processes were used. The position of best focus in the tool could change by as much as 100 nm, equivalent to 2 focus steps in the FEM. This magnitude of variance contributed to problems with capturing complete process windows for each wafer printed, and as can be seen in the analyzed data, some process windows were cut off in focus and dose.

Table 2. Experimental Measurements From Resist Printing on the MET

		Mask CD (nm at wafer)		Mask	$D_{size,V}$	Tool Best	DOF (nm) @8% EL		DOF (nm) @12% EL		Focus Shift	H-V CD Bias (nm)
afer	Mask Type	Horizontal	Vertical	Contrast	(mJ/cm^2)	Focus$_V$ (nm)	Horizontal	Vertical	Horizontal	Vertical	(nm) H - V	CD_H - $CD_{V\ @BD/BF}$
1	Cr/SiO_2	54.6	53.8	---	21.3	6299	192	191	---	---	-50	-1.2
2	Cr/SiO_2	54.6	53.8	---	17.3	6348	227	176	---	---	-30	-1.6
3	TaN/SiO_2	66.9	65.1	99.0%	21.0	6500	>300	>350	>269	304	-25	1.7
4	TaN/SiO_2	66.9	65.1	99.0%	19.9	6553	>290	>240	223	>240	-25	0.8
5	Etched Mo/Si	59.0	59.0	99.8%	21.9	6447	>195	193	76	---	-38	-2.0
6	Etched Mo/Si	59.0	59.0	99.8%	18.9	6346	214	240	---	119	-23	-2.8

Figure 9 displays SEM micrographs that qualitatively demonstrate the differences in through focus behavior of the 60 nm resolution elbows. Examples of Bossung plots for 60 nm horizontal lines, including polynomial fits calculated using the ProData (KLA Tencor) software package, are displayed in Figure 10 for each of the three EUV prototype photomasks. From Bossung curves, process windows were calculated using a 10% tolerance on the target CD for horizontal and vertical features printed with each mask using two replicate wafers per mask. The target mask CDs were measured on these reticles by SEM and analysis of micrographs were performed in SuMMIT. The mask CDs are listed in Table 2.

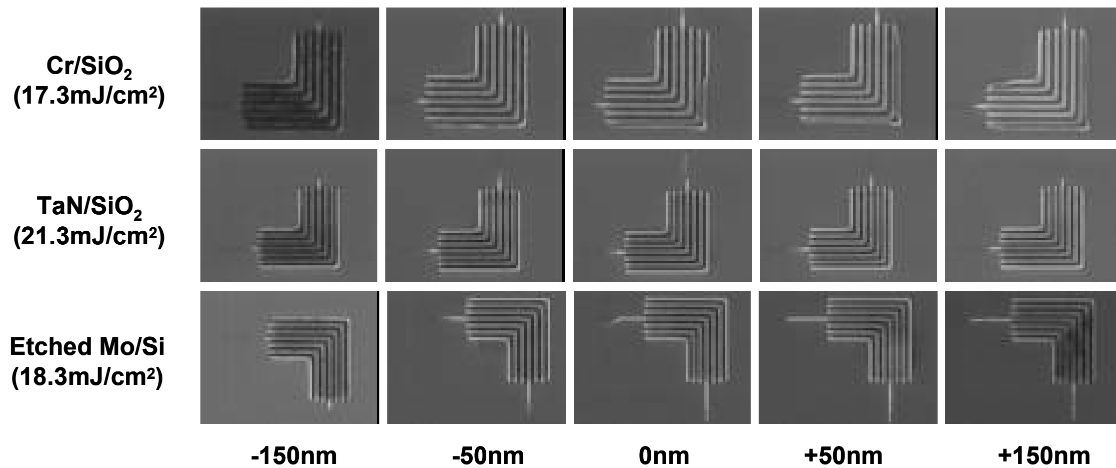

Figure 9. SEM micrographs of 60 nm lines and spaces printed in MET-1K photoresist using the Cr/SiO_2 (50kX magnification) and TaN/SiO_2 (40kX magnification) absorber masks and the etched multilayer mask (40kX magnification) at dose values close to D_{size} and various focus settings. Note the iso-dense bias is improved for the etched multilayer mask compared to absorber masks.

Table 2 lists the measured depth of focus (DOF) for each mask using 8% and 12% exposure latitude (EL). The data indicates a depth of focus greater than 240 nm for both horizontal and vertical lines using the TaN/SiO_2 absorber mask at 8% EL. Due to the limited focus range used in the experiment, the complete DOF at 8% EL could not be determined from either wafer. At 8% EL the etched multilayer mask exhibited the second largest DOF, but the Cr/SiO_2 absorber

mask was only slightly worse. Tightening the process window to a constraint of 12% EL brings some of the Bossung plots from the TaN/SiO_2 mask into the range of DOF used in the experiment, while some measurements remain cut off in focus. For the Cr/SiO_2 mask, the maximum EL at zero DOF was approximately 10%, so no process could be obtained at 12% EL. For the etched multilayer mask, 12% EL is at the limit of the process window obtained by the Bossung plots, resulting in mixed data due to fluctuations in the experimental data and the polynomial fitting methods used by ProData. Despite wafer-to-wafer variations and the cutoff of process windows in both focus and dose, a trend can be seen through the three mask types. The largest process windows are found for the TaN/SiO_2 absorber mask under these experimental conditions, followed by the etched multilayer mask and then the Cr/SiO_2 absorber mask. The large DOF measured using the TaN/SiO_2 absorber mask can be seen from SEM images through focus as shown in Figure 11.

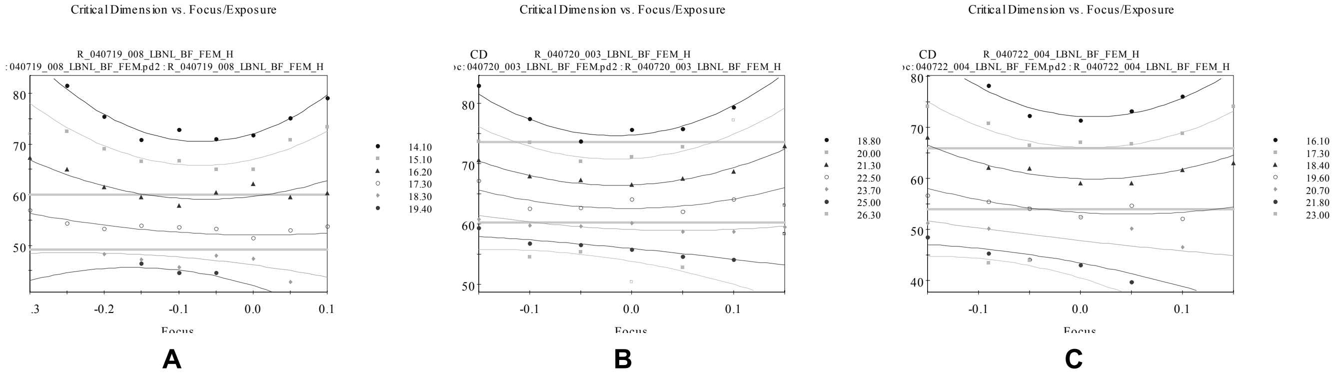

Figure 10. Bossung plots for 60nm horizontal lines for the a) Cr/SiO_2 (wafer2), b) TaN/SiO_2 (wafer 3), and c) etched multilayer (wafer 6) masks.

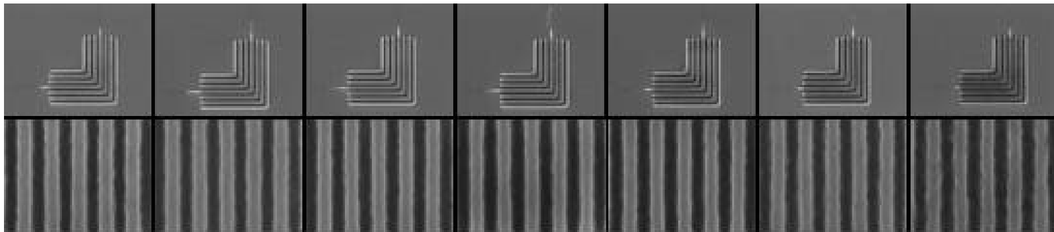

Figure 11. SEM micrographs of 60 nm elbows and vertical lines and spaces printed in MET-1K photoresist using the TaN/SiO_2 absorber mask (wafer 3) at a constant dose of 21.3 mJ/cm^2 through focus from –0.15 μm to +0.15 μm (left to right) in 50 nm steps.

Horizontal and vertical lines were found to have a shift in the position of best focus, with horizontal lines offset to negative values of focus (in the MET, negative defocus moves the wafer closer to the optics). The offset in focus was approximately ½ to 1 focus step in the experiment (25-50 nm), and is tabulated in Table 2. According to the levels of astigmatism measured in for the MET optic, about 50 nm of focus shift was expected between horizontal and vertical features.[22] The shift in best focus between horizontal and vertical features and the effects of mask shadowing by absorber topography will contribute to differences in CD. The CD offset between horizontal and vertical lines was measured from experimental data by the difference in resist CD of vertical lines at best focus and dose and the resist CD of the horizontal lines at the same values of focus and dose. The difference in mask CD between horizontal and vertical lines was used to correct the bias measurements, and data are provided in Table 2. The magnitude of H-V CD bias was small for all masks, and the uncertainty in the calculation is likely large due to the statistical fluctuations of measuring CDs in resist and on the masks, and the small sample size used. However, the trend between masks is consistent with expectations from simulations. The etched multilayer mask has a negative value of H-V bias, indicating vertical features

print larger than horizontal features by about 2 nm. This is consistent with previously published results from simulations that show about 2 nm larger CDs for vertical features compared to horizontal features. This is caused by the requirement that EUV light pass through a sufficient number of multilayer pairs in order to be reflected with significant intensity. Some intensity is lost at the edge of a horizontal features due to the oblique angle of incidence where light does not pass through a sufficient number of multilayer pairs, resulting in a smaller CD in resist. For the TaN absorber mask, the value for CD bias becomes positive, which indicates that horizontal lines print larger than vertical lines. This is consistent which expectations based on shadowing of the horizontal lines by the height of the mask absorber, leading to larger resist CDs for horizontal lines. The effect of shadowing for the TaN absorber film was expected to be larger than for the Cr absorber film due to its greater film thickness, and this trend is supported by the data.

5. DISCUSSION

The main challenge in comparing the imaging performance of different types of mask is to evaluate each of them under their own optimum condition. For dense lines, one should adjust the mask CD to print the targeted CD at the iso-focal dose so as to maximize the depth of focus. For a number of reasons, which include the largely unknown response of the MET-1K resist prior to this study, this was not done during these initial experiments. As can be seen in Table 3 below, the iso-focal CD for the three masks, as estimated from the Bossung plots shown in Figure 10, are all smaller than the targeted CD (CD_M) by 5 nm or more. Also tabulated are the simulated iso-focal CD values and the average difference between the measured iso-focal CDs and the simulated iso-focal CDs, which we call the intrinsic bias because of the well-known characteristic of positive-tone chemically amplified resist to print CDs smaller than predicted. This value of the intrinsic bias extracted from the experimental and simulations results is fairly consistent for all masks at about 17.5 nm on average.

Table 3. Estimation of the intrinsic bias for the resist MET-1K. The values of iso-focal CD extracted from the Bossung plots shown in Figures 8 and 11 indicate that the intrinsic bias of resist MET-1K is 17.5 nm on average and that it is fairly consistent for all masks patterned.

	Experimental Iso-focal CD (nm)		Simulated Iso-focal CD (nm)		Average
Mask type	Horizontal	Vertical	Horizontal	Vertical	Intrinsic Bias (nm)
Cr/SiO_2 (CD_M= 55nm)	50.5	49	65.6	66	16
TaN/SiO_2 (CD_M= 65nm)	56	54	72.6	71.4	17
Etched Mo/Si (CD_M= 60nm)	50.5	45.5	67	68	19.5

This offset between the iso-focal CD and the targeted CD is the biggest factor affecting the values of depth of focus extracted from the experimental data, and it is hiding the true potential of each of these masks. Once the intrinsic bias of the resist is known, it is possible to compensate for this effect in the simulations and provide a more meaningful comparison. This is done in the following way. First, imaging simulations are performed for each mask using the actual CD of the mask. Second, Bossung plots are generated as described in section 3. Third, values of the CD in the simulated Bossung plots are reduced by the average intrinsic bias. Finally, the process windows are evaluated using ProData. When this is done, the simulated depth of focus follows the same trend observed experimentally, with the TaN/SiO_2 mask having the largest depth of focus, followed by the etched multilayer mask, and then the Cr/SiO_2 mask.

By targeting the mask CD better, it should possible to operate at the iso-focal dose and improve the depth of focus for each of these masks. The sensitivity of the depth of focus to the dimension of the mask CD is evaluated in ProData by varying the target CD, assuming an exposure latitude of 10% and using the simulated Bossung plots corrected for the intrinsic bias. Although not rigorous, this procedure is roughly equivalent to evaluating depth of focus from a series of simulated Bossung plots corresponding to different mask CDs and using a constant target CD in ProData. The results of this exercise are plotted in Figure 12.

It is interesting to note that for the mask CDs used in the experiment, the simulated depth of focus of the etched multilayer mask is a strong function of the mask CD (around 59 nm) while that of the TaN/SiO_2 mask is not as sensitive to the mask CD (around 66 nm). This might explain that the data from the TaN/SiO_2 mask appeared to be more consistent than that of the etched multilayer mask.

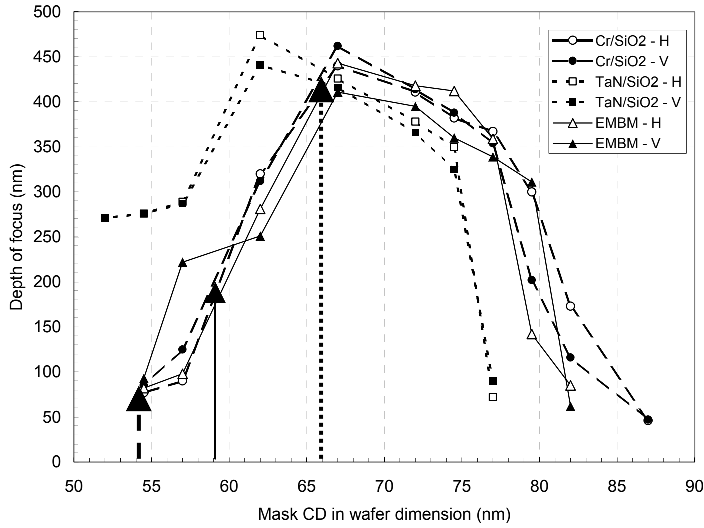

Figure 12. Sensitivity of the depth of focus of the masks under study to mask CD. Dashed lines represents the DOF for the Cr/SiO_2 mask (55 nm mask CD), the dotted lines correspond to the TaN/SiO_2 mask (65 nm mask CD), and the solid lines correspond to the etched multilayer mask (60 nm mask CD). The actual mask CDs used in this experiment are indicated with arrows and show that the simulated values for depth of focus follow the same trend as observed experimentally.

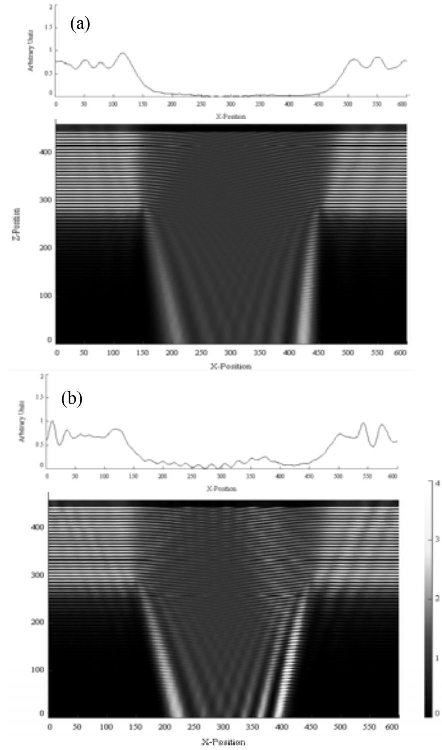

Figure 13. Near-field intensity cross-sections and profiles for the etched multilayer mask at two values of the sidewall angle: 90° and (b) 80°. The contrast achieved with the 90° sidewall is better.

From Figure 12, the optimum mask CD value should have been around 65 nm to 67 nm both for the Cr/SiO_2 mask and the etched multilayer mask, while a smaller mask CD (56 nm to 61 nm) would have been better for the TaN/SiO_2 mask. At the best mask CD value, the TaN/SiO_2 mask and the etched multilayer mask are almost equivalent, while the Cr/SiO_2 mask has a depth of focus that is smaller by about 100 nm compared to the other two.

This conclusion is not consistent with previous simulation work indicating that the etched multilayer mask should perform better than absorber masks.[1, 5] We believe that several factors might be contributing to this result. Here are two of the most important ones in our opinion. First, the current analysis is focused exclusively on dense feature. Previously published conclusions were based on the overlap process windows for at least three types of features, including an isolated line. A qualitative look at the isolated lines on the elbow patterns shown in Figure 9 tends to point to better results with the etched multilayer mask but one needs to be aware again of biasing effects before drawing definative conclusions from these images. Second, the etched multilayer mask used in this experiment has a sidewall of approximately 80°, which is not optimum. A comparison of the near-field intensity produced by an etched multilayer mask with 80° and 90° sidewall angles is shown in Figure 13. This clearly illustrates that the contrast achieved with the 90° sidewall is better and should lead to better process latitude.

6. CONCLUSION

We have followed a path to evaluate the benefits of various mask architectures for EUVL that originates with the fabrication of prototype photomasks and ends with the analysis of data obtained from printing these masks at EUV. The nature of experiments using pre-manufacturing EUV lithography tools with prototype masks and experimental photoresists makes decisive, conclusive results difficult to obtain, however our understanding of the critical parameters for optimizing EUV mask architecture continues to grow. Our first round of printing experiments on the MET validated several trends observed in simulation. Bias between horizontal and vertical lines due to shadowing appears to be

consistent with expectations from simulation. Process latitude for all mask architectures depends strongly on mask bias. Future experiments must be designed to allow for easy investigation of biasing mask CDs, and printing results must capture the iso-focal condition in order to account for intrinsic bias of a chemically amplified resist.

ACKNOWLEDGEMENTS

The authors thank Paul Denham for assistance with the patterning experiments using these masks on the EUV microexposure tool at Lawrence Berkeley National Lab. Georgia Rich of International SEMATECH is thanked for her assistance in reticle SEM measurements. Kim Dean of International SEMATECH is thanked for her continuous assistance in planning and project management aspects required by this work.

REFERENCE

[1] Y. Deng, B. M. L. Fontaine, H. J. Levinson, and A. R. Neureuther, "Rigorous EM simulation of the influence of the structure of mask patterns on EUVL imaging," *Proc. of SPIE, Emerging Lithographic Technologies VII*, vol. 5037, pp. 302-313, 2003.

[2] M. Sugawara, A. Chiba, and I. Nishiyama, "Effect of incident angle of off-axis illumination on pattern printability in extreme ultraviolet lithography," *Journal of Vacuum Science & Technology B: Microelectronics and Nanometer Structures*, vol. 21, pp. 2701-2705, 2003.

[3] C. G. Krautschik, M. Ito, I. Nishiyama, and T. Mori, "Quantifying EUV imaging tolerances for the 70-, 50-, 35-nm modes through rigorous aerial image simulations," *Proc. of SPIE, Emerging Lithographic Technologies V*, vol. 4343, pp. 524-534, 2001.

[4] B. L. Fontaine, A. R. Pawloski, Y. Deng, C. Chovino, L. Dieu, O. R. W. II, and H. J. Levinson, "Architectural choices for EUV lithography masks: patterned absorbers and patterned reflectors," *Proc. of SPIE, Emerging Lithographic Technologies VIII*, vol. 5374, pp. 300-310, 2004.

[5] Y. Deng, B. L. Fontaine, A. R. Pawloski, and A. R. Neureuther, "Simulation of fine structures and defects in EUV etched multilayer masks," *Proc. of SPIE, Emerging Lithographic Technologies VIII*, vol. 5374, pp. 760-769, 2004.

[6] S. D. Hector, "EUVL masks: requirements and potential solutions," *Proc. of SPIE, Emerging Lithographic Technologies VII*, vol. 4688, pp. 134-149, 2002.

[7] P.-y. Yan, "Impact of EUVL mask buffer and absorber material properties on mask quality and performance," *Proc. of SPIE, Emerging Lithographic Technologies VIII*, vol. 4688, pp. 150-160, 2002.

[8] P. J. S. Mangat, S. D. Hector, M. A. Thompson, W. J. Dauksher, J. Cobb, K. D. Cummings, D. P. Mancini, D. J. Resnick, G. Cardinale, C. Henderson, P. Kearney, and M. Wedowski, "Extreme ultraviolet lithography mask patterning and printability studies with a Ta-based absorber," presented at Papers from the 43rd international conference on electron, ion, and photon beam technology and nanofabrication, Marco Island, Florida (USA), 1999.

[9] T. Shoki, T. Kinoshita, N. Sakaya, M. Hosoya, R. Ohkubo, Y.-i. Usui, H. Kobayashi, and O. Nagarekawa, "Damage-free extreme ultraviolet mask with TaBN absorber," *Journal of Vacuum Science & Technology B: Microelectronics and Nanometer Structures*, vol. 21, pp. 3021-3026, 2003.

[10] Y. Tanaka, D. Kim, H. Yamanashi, and I. Nishiyama, "EUV absorbance and dry-etching characteristics of TaGeN films for EUVL mask absorber," *Proceedings of SPIE-The International Society for Optical Engineering*, vol. 5374, pp. 281-288, 2004.

[11] J. R. Wasson, E. J. Weisbrod, B. Lu, P. J. S. Mangat, W. J. Dauksher, D. J. Resnick, J. Sohn, R. Engelstad, and D. Pettibone, "Extreme ultraviolet mask fabrication with high inspection contrast TaSiN[sub x] absorber stack," *Journal of Vacuum Science & Technology B: Microelectronics and Nanometer Structures*, vol. 21, pp. 3086-3090, 2003.

[12] P.-y. Yan, G. Zhang, A. Ma, and T. Liang, "TaN EUVL mask fabrication and characterization," *Proc. of SPIE, Emerging Lithographic Technologies V*, vol. 4343, pp. 409-414, 2001.

[13] G. Zhang and P.-y. Yan, "Cr and TaN Absorber Mask Etch CD Performance Study For Extreme Ultraviolet Lithography," *Proc. of SPIE, 22nd Annual BACUS Symposium on Photomask Technology*, vol. 4889, pp. 1092-1098, 2002.

[14] *EUV Technology, http://www.euvl.com/summit.*

[15] *Panoramic Technology, http://www.panoramictech.com.*

[16] K. A. Goldberg, P. Naulleau, P. Denham, S. B. Rekawa, K. Jackson, J. A. Liddle, and E. H. Anderson, "EUV interferometric testing and alignment of the 0.3-NA MET optic," *Proc. of SPIE, Emerging Lithographic Technologies VIII*, vol. 5374, pp. 64-73, 2004.

[17] *X-ray interactions with matter, http://www-cxro.lbl.gov/optical_constants/.*

[18] P. Naulleau, K. A. Goldberg, E. H. Anderson, K. Bradley, R. Delano, P. Denham, B. Gunion, B. Harteneck, B. Hoef, H. Huang, K. Jackson, G. Jones, D. Kemp, J. A. Liddle, R. Oort, A. Rawlins, S. Rekawa, F. Salmassi, R. Tackaberry, C. Chung, L. Hale, D. Phillion, G. Sommargren, and J. Taylor, "Status of EUV micro-exposure capabilities at the ALS using the 0.3-NA MET optic," *Proc. of SPIE, Emerging Lithographic Technologies VIII*, vol. 5374, pp. 881-891, 2004.

[19] P. Naulleau, K. A. Goldberg, J. P. Cain, E. Anderson, P. Denham, K. Jackson, S. Rekawa, F. Salmassi, and G. Zhang, "EUV Microexposures at the ALS Using the 0.3NA MET Optic," presented at The 48th international conference on electron, ion, and photon beam technology and nanofabrication, San Diego, CA (USA), 2004.

[20] R. L. Brainard, C. Henderson, J. Cobb, V. Rao, J. F. Mackevich, U. Okoroanyanwu, S. Gunn, J. Chambers, and S. Connolly, "Comparison of the lithographic properties of positive resists upon exposure to deep- and extreme-ultraviolet radiation," *Journal of Vacuum Science & Technology B*, vol. 17, pp. 3384-3389, 1999.

[21] S. A. Robertson, P. P. Naulleau, D. J. O'Connell, K. McDonald, T. M. Delano, K. A. Goldberg, S. G. Hansen, K. W. Brown, and R. L. Brainard, "Calibration of EUV 2D photoresist simulation parameters for accurate predictive modeling," *Proc. of SPIE, Emerging Lithographic Technologies VII*, vol. 5037, pp. 900-909, 2003.

[22] P. Naulleau, "unpublished work," 2004.